

16

Accurate Kohn–Sham DFT With the Speed of Tight Binding: Current Techniques and Future Directions in Materials Modelling

Patrick R. Briddon and Mark J. Rayson

16.1

Introduction

The Kohn–Sham formalism [1] of density functional theory [2] (KSDFT) is one of the most widely used tools in the *ab initio* theoretical investigation of the properties of materials. Its success at providing quantitative comparison with experiment—given only atomic positions and species as input—combined with its favourable algorithmic prefactor and complexity accounts for this widespread usage and intensive efforts to improve the algorithms at the heart of KSDFT codes.

Here we describe how recent algorithmic advances in the computational kernel at the heart of one of these codes, *Ab Initio* Modelling PROgram (AIMPRO), will enable a new scale of calculation to be performed on inexpensive hardware. The modern algorithmic kernel, functionality, current advances and future perspectives will be discussed. In short, the aim of this work is to show how full KSDFT calculations can be performed in a time comparable to current tight binding implementations and further, to open a route to reaching the basis set limit in these calculations, essentially delivering plane wave accuracy in a time comparable to a tight binding calculation. In the following discussions we define the Kohn–Sham kernel as the calculation of energies and forces, leading to minimum energy structures (including lattice optimisation). Any other calculated quantity will be referred to as functionality. Readers interested in the details of algorithms used in the AIMPRO suite of codes are referred to Refs. [3–9].

As well as a description of the algorithms we also wish to address the wider audience of applications specialists. By discussing recent advances in terms of both their methodological context and relevance to the practitioner we hope this work will be of interest to a wide audience.

This chapter is organised as follows, Section 16.2 discusses the use of Gaussian orbitals and briefly describes the conventional AIMPRO kernel, Section 16.3 gives a brief overview of the functionality currently available, Section 16.4 describes recent improvements to the AIMPRO kernel and Section 16.5 discusses future research

directions and perspectives based on recent advances. Readers familiar with conventional Gaussian algorithms, or those interested primarily in recent advances in the kernel, can skip straight to Section 16.4.

16.2

The AIMPRO Kohn–Sham Kernel: Methods and Implementation

In this section we briefly outline the major steps involved in a conventional electronic structure code, introducing notation that is needed when new innovations are introduced later.

The standard approach is to expand the Kohn–Sham levels in terms of basis function, $\phi_i(\mathbf{r})$:

$$\psi_\lambda(\mathbf{r}) = \sum_{i=1}^N c_{i\lambda} \phi_i(\mathbf{r}), \quad (16.1)$$

which enables the Kohn–Sham equations to be recast in matrix form:

$$\sum_j H_{ij} c_{j\lambda} = \epsilon_\lambda \sum_j S_{ij} c_{j\lambda} \quad \text{or} \quad \mathbf{H}\mathbf{c} = \mathbf{S}\mathbf{c}\Lambda, \quad (16.2)$$

where $\Lambda_{\lambda\lambda'} = \epsilon_\lambda \delta_{\lambda\lambda'}$.

In this way the electronic structure problem is reduced into three components. The first is essentially one of quadrature, determining the Hamiltonian and overlap matrices:

$$\begin{aligned} H_{ij} &= \int \phi_i^*(\mathbf{r}) \hat{H} \phi_j(\mathbf{r}) d\mathbf{r}; \\ S_{ij} &= \int \phi_i^*(\mathbf{r}) \phi_j(\mathbf{r}) d\mathbf{r}. \end{aligned} \quad (16.3)$$

The second problem is the solution of the generalised eigenvalue problem (GEP) [Eq. (16.2)]. This will occupy discussion for the majority of this chapter, being the most computationally expensive part of the calculation. The final ingredient, which is not discussed in this chapter, is a method of iterating to self-consistency.

16.2.1

Gaussian-Type Orbitals

Uncontracted Cartesian Gaussian functions

$$\phi_i(\mathbf{r}) = (x - R_{ix})^{n_x} (y - R_{iy})^{n_y} (z - R_{iz})^{n_z} \exp[-a_i(\mathbf{r} - \mathbf{R}_i)^2]$$

are used to form our primitive set. For each atom, we typically use four different exponents a_i and we multiply each Gaussian function $\exp[-a_i(\mathbf{r} - \mathbf{R}_i)^2]$ by the Cartesian prefactors, including all combinations of n_x , n_y and n_z such that $n_x + n_y + n_z \leq \ell$. This produces four functions for $\ell = 1$ and ten functions for $\ell = 2$.

In our notation, exponents are arranged from lowest to highest (most diffuse Gaussian first) and the standard nomenclature is used to define the angular momentum. So, for example a *ddpp* basis has four exponents with $10 + 10 + 4 + 4 = 28$ functions. Such a basis set applied to carbon or silicon would be considered large for a routine quantum chemistry application.

We now consider the advantages and disadvantage of using Gaussian orbitals.

Advantages:

- i) Memory. The size of the primitive basis is small, typically only 20–40 functions per atom. Furthermore, the storage of a primitive basis function requires only 3 integers and 2 double precision numbers.
- ii) Adaptive. Basis functions can be placed where they are most needed.
- iii) Gaussian functions are localised in both real and Fourier space and careful use of this fact enables matrix elements of the Hamiltonian to be found extremely efficiently (see Section 16.2.2).
- iv) The integration error is independent from basis error leading to an internally consistent calculation. That is, even with a large basis error the matrix elements of the Hamiltonian are still evaluated to high precision. This is important when considering relative energies.

Adaptivity, coupled with rapid matrix element evaluation, allows chemical species with hard potentials to be treated almost as easily as species with soft potentials. Therefore, a single oxygen or hydrogen (typically having hard pseudopotentials) embedded in, say, a unit cell containing 1000 atoms of silicon (which has a fairly soft pseudopotential) would take a similar time to 1000 atoms of silicon.

Disadvantages:

- i) Basis set superposition error (BSSE).
- ii) Difficulty in running codes—a degree of experience is currently needed to choose a suitable basis set.
- iii) Difficulty in proving convergence.

The main disadvantage is related to the relative complexity of the Gaussian basis set and the less obvious way in which basis sets can be augmented to move towards convergence in energy or some other property. Large basis sets generated to minimise the energy of a system can develop numerical linear dependencies as convergence is approached, with the result that a certain level of skill and experience is needed to work in this regime. The work in this chapter provides a first step to removing this as a legitimate concern.

It is important to note the effect of BSSE depends on the quantity of interest. When interested in relative energies the degree of difference between the systems must be considered. Therefore, two very different systems will suffer most from BSSE when considering their relative energy. Not quite as challenging is a calculation such as the formation energy of a vacancy—here the systems are fairly similar—though the vacancy calculation has fewer degrees of freedom, therefore this is a problem of intermediate difficulty. However, a slight perturbation of an atom (such as a numerical force calculation) will suffer far less from BSSE, this will be discussed

further and demonstrated in Section 16.4.2. Since the large majority of computer time is spent in structural relaxations (and other quantities where derivatives of the energy are of paramount importance) a significant amount of computer time can be saved by correctly assessing the relevant impact of BSSE on a calculation. Although, at present, much of this must be done by the user, in principle, it can be automated. We will discuss work in this direction in Section 16.5.

16.2.2

The Matrix Build

The building of the Hamiltonian is achieved using standard techniques. The overlap matrix, and the matrix elements of kinetic energy and the non-local pseudopotential may be found analytically using recurrence relations reported in Ref. [10]. The matrix elements of the Kohn–Sham potential are found as described in Refs. [6] and [11].

An important difference between our approach and standard methods of quantum chemistry is our avoidance of four centre integrals. Our approach of quadrature using a set of equally spaced grids [6] has linear scaling with an acceptable prefactor. In doing this the charge density and the potential are expressed on an equally spaced grid in real space which, in plane wave parlance would have an exceptionally high cutoff—typical values would be 80 Rydbergs (silicon) and 300 Rydbergs (carbon). This is feasible as this expansion is done only for the charge density, and not for each individual Kohn–Sham level. A consequence is that the Hamiltonian matrix is determined essentially free of integration error, with arbitrarily high accuracy being achievable at modest cost. Timings for this are presented in passing in Section 16.4.1 when it is noted that this is a negligible contribution to run-times for large systems, being only 3 min when run in serial on a single core even for a system of 4096 atoms.

16.2.3

The Energy Kernel: Parallel Diagonalisation and Iterative Methods

Once the primitive Hamiltonian and overlap matrices—**H** and **S** respectively—have been evaluated these are then converted from sparse storage to a dense block-cyclic parallel distribution. The $N \times N$ GEP

$$\mathbf{H}\mathbf{c} = \mathbf{S}\mathbf{c}\Lambda, \quad (16.4)$$

is then solved (ScaLAPACK diagonalisation) to calculate the output density

$$n(\mathbf{r}) = \sum_{ij} b_{ij} \phi_i(\mathbf{r}) \phi_j(\mathbf{r}), \quad (16.5)$$

where

$$b_{ij} = \sum_{\lambda}^m f(\Lambda_{\lambda\lambda}) c_{i\lambda} c_{j\lambda}, \quad (16.6)$$

and m is the number of occupied states. A charge density mixing scheme [12] is used to iterate (the ‘SCF cycle’) towards the self-consistent density.

As well as diagonalisation, especially when the N/m ratio is high and good parallel scaling is important, an iterative algorithm—based on the direct inversion of the iterative subspace (DIIS)—is also used [5].

16.2.4

Forces and Structural Relaxation

It is occasionally argued that the determination of forces is more complex and time consuming with Gaussian orbitals as a consequence of the Pulay forces associated with atom centred basis functions. This, in fact, is not the case in reality. In fact, viewing Pulay forces as an approximation to incompleteness forces (see Section II C of Ref. [6] for a detailed discussion) it is more accurate to say that rather than being a burden, the ability to calculate Pulay forces (rather than their presence) is a distinct advantage as significant efficiencies can be obtained (see Section 16.4 for a more detailed discussion).

Forces are determined from the Hellmann–Feynman theorem as adapted for localised basis functions [3]:

$$\frac{\partial E}{\partial \mathbf{R}_\alpha} = \sum_{ij} \frac{\partial H_{ij}}{\partial \mathbf{R}_\alpha} b_{ij} - \sum_{ij} \frac{\partial S_{ij}}{\partial \mathbf{R}_\alpha} w_{ij},$$

where w_{ij} is the energy weighted density matrix

$$w_{ij} = \sum_{\lambda}^m f(\Lambda_{\lambda\lambda}) \Lambda_{\lambda\lambda} c_{i\lambda} c_{j\lambda}. \quad (16.7)$$

The first term, $\frac{\partial H_{ij}}{\partial \mathbf{R}_\alpha} b_{ij}$, is trivially evaluated in time scaling linearly with system size. Indeed the time for this is only marginally greater than the construction of the Hamiltonian itself, only ~ 45 s for a 1000 atom cell (see discussion of timings in Section 16.4.1). The construction of w_{ij} is likewise straightforward. Evaluating Eq. (16.7) directly using $\mathcal{O}(N^3)$ dense matrix operations imposes a negligible overhead—and, in principle, since only elements of w_{ij} that have corresponding non-zero elements in the Hamiltonian are required this step can be performed in $\mathcal{O}(N^2)$. In conclusion then, force determination is possible in a small fraction of the time for a single SCF step.

Movement of the atoms to attain equilibrium is then achieved using any standard scheme. We commonly use the conjugate gradient method [13], BFGS [13] and G-DIIS methods [14].

16.2.5

Parallelism

AIMPRO is parallelised using the message passing interface library (MPI). A library to handle the creation and destruction of multiple worlds—and levels of worlds—is

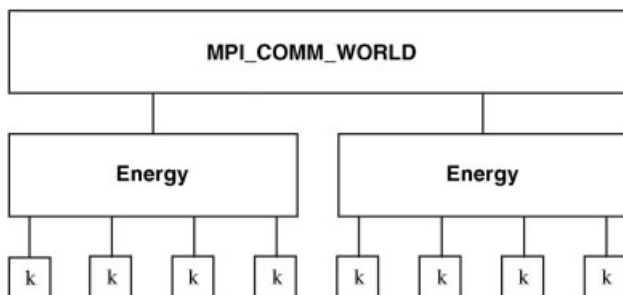


Figure 16.1 Schematic of parallel worlds (see text for details).

also implemented. A typical arrangement of these worlds for the calculation of the dynamical matrix is given in Figure 16.1. Each ‘Energy world’ could, for example, calculate a row of the dynamical matrix, furthermore within each energy calculation the calculation can further be split into separate ‘k-point worlds’. Such flexible infrastructure such as this enables extra ‘embarrassingly parallel’ functionality to be included in the main algorithm itself.

16.3

Functionality

Although in this chapter, the emphasis is on the kernel of the calculation, and how this may be improved both in terms of speed and accuracy, the great utility of *ab initio* calculations over the last two decades has been their ability to link to an increasingly broad range of experiments, producing quantitatively accurate values for measurable quantities. In this section, we illustrate this by outlining some of the functionality incorporated into the AIMPRO code and the problems tackled.

16.3.1

Energetics: Equilibrium and Kinetics

The fundamental property given by these calculations is, of course, the total energy. In terms of defect physics, this is of outstanding importance with the formation energy controlling the equilibrium concentrations of defects. The energy barrier to motion of a defect through a material, gives information about kinetic motion and is as important as the formation energy in understanding the behaviour of defects in a material. For example, the result that the diffusion barrier of hydrogen in ZnO is under 0.5 eV has demonstrated that isolated H cannot be responsible for the residual *n*-type conductivity of this material [15] as had previously been thought. On the other hand, the fact we can show that H binds strongly to other impurities to produce thermally stable complexes can provide alternative explanations for this phenomena [16] and can also have important technological implications for other doping issues [17].

It is frequently the energetics of defects at the high temperatures at which material processing occurs that can determine the defects seen in materials. As such a free energy of formation should be calculated at the temperature at which the material is processed. Calculations of this requires treatment of vibrational modes for all atoms in a unit cell, once demanding but now becoming a more common calculation. It can often happen that a binding energy changes sign at high temperature leading to some defect complexes being absent in samples [18].

16.3.2

Hyperfine Couplings and Dynamic Reorientation

An accurate knowledge of the electron spin density enables the coupling with the magnetic moment of certain nuclei to be calculated, enabling a comparison with experimentally measured hyperfine coupling tensors. In the simplest case a comparison with experiment can be a powerful tool enabling the characterisation of defect centres [19]; in more complex cases low symmetry defects can re-orient dynamically at room temperature appearing experimentally as having a higher symmetry. In this case the ability to calculate both the energy barrier and the averaged hyperfine tensor is key [19]. The physics here is quite rich in variety with quantum tunnelling of hydrogen also being demonstrated [20].

16.3.3

D-Tensors

Defects with electron spin, $S > 1$ exhibit a zero field splitting, measured experimentally as the D-tensor. A method to calculate the first order contribution to the zero-field splitting tensor was presented in Ref. [9]. Again comparison of calculated tensors [21–25] with experiment aids in the characterisation of defect centres. The ability to perform a quantitative calculation has also shown that conclusions drawn from the phenomenological point dipole model frequently used to interpret the size of the D-tensor are not always reliable [21].

16.3.4

Vibrational Modes and Infrared Absorption

The vibrational modes associated with defects are readily measured experimentally, and may be calculated from the second derivatives of the energy surface. These modes have been some of the most fruitful methods of characterising defects [26, 27].

16.3.5

Piezospectroscopic and Uniaxial Stress Experiments

Calculation of piezospectroscopic (energy–stress) tensors of defects also provides a direct link with experiment [28]. The response of vibrational frequencies to uniaxial

stress is also a valuable tool in the experimental determination of defect symmetry and these shifts can be calculated accurately from total energy calculations, providing a further aid in characterisation studies [29].

16.3.6

Electron Energy Loss Spectroscopy (EELS)

The simplest treatment of energy loss spectroscopies is based on the dipole matrix elements between Kohn–Sham states. This is an approximate model, but in many instances is sufficiently accurate for features in experimental spectra to be correlated with electronic states associated with regions of defects, particularly extended defects. Both low-loss [30, 31] and core–electron energy loss spectroscopy (EELS) experiments (or the theoretically similar XPS experiment [32]) can be modelled.

16.4

Filter Diagonalisation with Localisation Constraints

We now turn to the main topic of this chapter, namely, recent advances in the KSDFT kernel that enable such calculations to be performed in a time comparable to a tight binding calculation. The conventional AIMPRO kernel described in Section 16.2 has been dramatically improved upon recently [6]. The filter diagonalisation method with localisation constraints promises to allow calculations with larger primitive sets, thereby approaching the basis set limit, while the fundamental density matrix is only the size of a minimal (or tight binding like) basis density matrix. For a detailed account of the method and algorithmic details the interested reader is referred to Refs. [6, 7]. Here, we summarise the method to elucidate later discussions, however, it is the broader impact of the filtration algorithm we wish to concentrate upon.

Rather than a direct diagonalisation in the full primitive basis a subspace eigenproblem is constructed in a small basis of filtered functions, defined in terms of the primitive basis set $\{\phi_i\}$ as

$$\Phi_I(\mathbf{r}) = \sum_i k_{iI} \phi_i(\mathbf{r}). \quad (16.8)$$

For silicon, for example, using the pseudopotential approximation this reduces the size of the kernel eigenproblem from, say, ~ 28 (if using the *ddpp* basis described in Ref. [6]) functions per atom to only four functions per atom—a significant saving. The step that performs this reduction in basis size will be referred to as the filtration algorithm. A filtration radius (r_{cut}) is defined and the filtered basis on an atom at \mathbf{R}_α constructed using basis functions that lie on atoms at \mathbf{R}_β where $|\mathbf{R}_\alpha - \mathbf{R}_\beta| < r_{\text{cut}}$. Henceforth, filtered basis sets will be referred to using the notation $\{\Phi^{(r_{\text{cut}})}\}$. A schematic of the filtration region for an atom is shown in Figure 16.2.

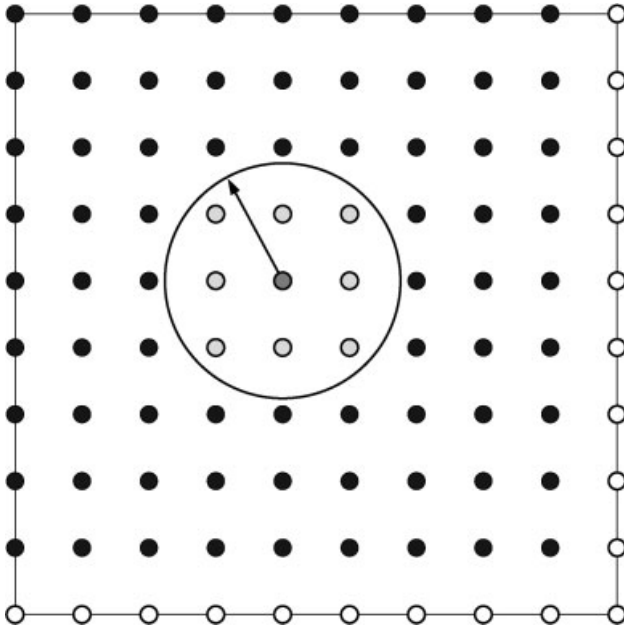


Figure 16.2 (online colour at: www.pss-b.com/) Schematic of the filtration region. Filled circles represent atoms and unfilled their periodic images. The green circle represents an

atom for which filtered functions are to be calculated and the yellow circles represent atoms whose primitive functions will contribute to these filtered functions.

The filtration step, as outlined in Ref. [6], consists of the following operations on a trial function $|\tilde{t}\rangle$

$$|\tilde{k}\rangle = cf(\Lambda)c^T S|\tilde{t}\rangle, \quad (16.9)$$

to obtain the vector of contraction coefficients $|\tilde{k}\rangle$. The remaining quantities are defined by the GEP

$$Hc = Sc\Lambda, \quad (16.10)$$

where, here, H and S matrices only consisting of a subset of the rows and columns of the Hamiltonian and overlap matrix formed in the large primitive basis (see Ref. [6]). In other words they are the H and S matrices associated with the primitive functions within the filtration region (Figure 16.2). The filtration function f used in Ref. [6] and throughout this work is a high temperature ($kT \sim 3$ eV) Fermi-Dirac function, which has the desired effect of removing the unnecessary high eigenspace of the Hamiltonian. The GEP [Eq. (16.10)] can be transformed to an ordinary eigenproblem

$$\bar{H}\bar{d} = L^{-1}HL^{-T}\bar{d} = \bar{d}\Lambda, \quad (16.11)$$

where \mathbf{L} is a lower triangular matrix and

$$\mathbf{S} = \mathbf{L}\mathbf{L}^T \text{ and } \mathbf{d} = \mathbf{L}^T \mathbf{c}. \quad (16.12)$$

From this we can express Eq. (16.9) as

$$|\tilde{k}\rangle = \mathbf{L}^{-T} \mathbf{d} f(\Lambda) \mathbf{d}^T \mathbf{L}^T |\tilde{t}\rangle = \mathbf{L}^{-T} f(\tilde{\mathbf{H}}) \mathbf{L}^T |\tilde{t}\rangle. \quad (16.13)$$

The primitive space \rightarrow subspace transformation is performed using the following sparse matrix multiplications;

$$\tilde{\mathbf{H}} = \mathbf{k}^T \mathbf{H} \mathbf{k} \text{ and } \tilde{\mathbf{S}} = \mathbf{k}^T \mathbf{S} \mathbf{k}. \quad (16.14)$$

From this one obtains the subspace GEP

$$\tilde{\mathbf{H}} \tilde{\mathbf{c}} = \tilde{\mathbf{S}} \tilde{\mathbf{c}} \tilde{\Lambda}. \quad (16.15)$$

Since the dimension of this eigenproblem is small—essentially the size of a tight binding Hamiltonian—it is, at present, solved with standard direct diagonalisation. However, it must be stressed that due to the filtered functions being localised this matrix will be sparse for large systems, and therefore alternatives to diagonalisation may be considered. After the solution of this eigenproblem is obtained the subspace density matrix is constructed

$$\tilde{b}_{IJ} = \sum_{\lambda} f(\Lambda_{\lambda\lambda}) \tilde{c}_{I\lambda} \tilde{c}_{J\lambda}, \quad (16.16)$$

after which the subspace \rightarrow primitive space transformation is performed

$$\mathbf{b} = \mathbf{k} \mathbf{b} \mathbf{k}^T, \quad (16.17)$$

and the calculation proceeds as normal. For calculations in silicon and similar materials we have used four functions produced using trial functions of s , and p type symmetry. The resulting functions $|\tilde{k}\rangle$ are plotted in Figure 16.3.

We should note that, although the number of functions we are using (four) has an obvious chemical significance for silicon, this is in no way a restriction of the algorithm. Indeed, we may choose to use more or less functions, with full convergence to the primitive basis being obvious as more functions are added. Using fewer than four functions can also give good results, but only if the filtration is performed at a low-enough temperature to permit this. Indeed, zero temperature filtration can produce an exact result with only two filtered functions per silicon atom, although this would not be practical as the functions would lose their localisation (in general), thereby removing any advantage of this method.

16.4.1

Performance

We now detail the performance of the current algorithm including latest developments [7] and also some very encouraging preliminary results from further

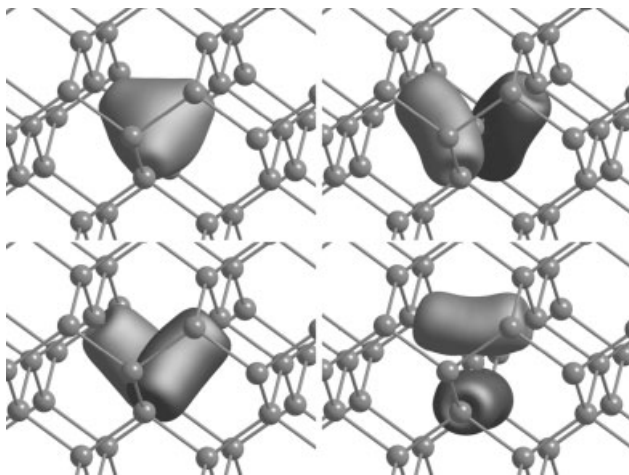


Figure 16.3 (online colour at: www.pss-b.com) Filter functions from trial functions of s , p_x , p_y and p_z (clockwise from top-left) symmetry.

optimisations of the algorithm. As a model system we look at unit cells of silicon created by forming $n \times n \times n$ arrays of the eight atom conventional unit cell, where $2 \leq n \leq 8$. It must be stressed, however, that the algorithm is not limited to wide-gap systems and is equally applicable to metals [6, 33]. The calculations use gamma point sampling and are performed on a single core of a 2.8 GHz Intel Xeon CPU.

Table 16.1 gives timings using an approximate filtration strategy—still good enough to give only a $\sim 10^{-4}$ Å error in relaxed final structures (see Section 16.4.2). Times are given for a single self-consistent iteration. For this system, SCF cycles

Table 16.1 Timings (s) of components of a self-consistent iteration for n^3 (simple cubic) cells of silicon ($n = 2, \dots, 8$) on a single 2.8 GHz Intel Xeon core. The first row gives the number of atoms in each cell. See Sections 16.2 and 16.4 for a description of the algorithmic components. These calculations correspond to the approximate filtration scheme (see Table 16.2).

	64	216	512	1000	1728	2744	4096
matrix build	2.79	9.38	22.99	45.05	76.48	133.99	185.11
potential calculation	0.07	0.22	0.58	1.15	2.11	3.44	4.84
filtration kernel	2.00	6.74	16.00	31.19	53.94	85.97	128.12
primitive \rightarrow subspace	0.48	3.82	12.41	27.61	48.76	77.71	116.10
subspace diagonalisation	0.03	0.47	7.73	52.58	270.63	1057.98	3740.67
density matrix build	0.00	0.07	0.86	6.11	31.88	124.13	414.33
subspace \rightarrow primitive space	0.11	0.96	5.35	24.88	72.30	138.89	213.17
calculation of real space density	0.43	1.53	3.75	7.42	12.75	21.97	30.51
overhead	0.11	0.70	1.85	3.20	7.56	11.59	19.14
total	6.02	23.89	71.52	199.19	576.41	1655.67	4851.99

require fewer than ten iterations to converge the Hartree energy associated with the difference of input and output densities to less than 10^{-5} Ha. The most notable detail in the table is the bottom line. This shows that on a single core a self-consistency step for a 1000 atom system takes just 200 s and a 1728 atom system less than 10 min. Therefore initial total energies of these systems can be found in ~ 30 min and ~ 1.6 h respectively. Clearly, even modest parallelism over the 8 cores, which may typically be in a commodity dual processor PC, reduces these to remarkably small values, and enable even complex structural relaxations on inexpensive hardware.

Clearly for small systems (*e.g.* 216 atoms) the dominant time is that of the matrix build [Eq. (16.3)] together with the filtration kernel [Eq. (16.9)]. These have $O(N)$ complexity and are clearly unimportant for larger systems where the $O(N^3)$ subspace diagonalisation begins to dominate. One somewhat surprising feature of the timings is that the primitive to subspace transformation [Eq. (16.14)] and its inverse [Eq. (16.17)] are not significant at any system size, occupying at most 20% of the total time (in 216 atoms) and gradually reducing for larger systems. This is a consequence of the sparsity of \mathbf{k} , \mathbf{H} and \mathbf{S} being well exploited together with reasonably efficient code (which achieves $\sim 25\%$ of peak performance) to perform the block-multiplications.

As a final comment, it is seen that for the 1728 atom system, approximately half of the total time is spent solving the subspace matrix eigenvalue problem. As the size of this matrix is the same as in a tight binding calculation it may be supposed that an accurate full DFT calculation on this system size may be performed in twice the time of a tight binding calculation. The difference however diminishes to just 20% for the 4096 atom system and asymptotically will vanish entirely, if direct diagonalisation is used in both.

16.4.2

Accuracy

We now analyse the accuracy of the filtration method by comparing formation energies and relaxed structures to the parent primitive basis. The filtration algorithm has been previously shown to produce energies and forces which are in close agreement with those produced by the conventional algorithm [6]. We have subsequently looked at a variety of different systems including metals and wide band gap materials [33]. In this section some further results are given focusing particularly on the accuracy of equilibrium structures and the impact of filtration on the atomic co-ordinates.

We first present a comparison of the structures of single interstitial atoms in silicon. Three structures are presented: the 110 defect in which a pair of Si atoms straddle a lattice site, displaced from it in $\langle 110 \rangle$ directions; an atom placed at a tetrahedral interstitial site (T_d in the table below), and a hexagonal interstitial site, labelled H in the tables. The calculations were performed in unit cells containing 217 silicon atoms, using a *ddpp* primitive basis, the pseudopotentials of Hartwigsen *et al.* [34] and k-point sampling corresponding to $2 \times 2 \times 2$ Monkhorst–Pack grid [35].

Structures were optimised until all components of forces on atoms were less than 5×10^{-5} a.u.

Two filtration conditions were chosen. The first uses a cutoff radius of 12 a.u., our standard converged value for silicon as used in previous work [6]. For this, Table 16.2 illustrates the minimal impact filtration has on equilibrium structure, with maximum deviations from the unfiltered results of order 10^{-4} Å or less. To further illustrate the insensitivity of the structures produced by filtration, a second filtration strategy was adopted which used a smaller localisation radius (10 a.u.) together with an more approximate filtration kernel. This more approximate approach shifts the total energy of the system by 0.3 Ha, an immense change but the corresponding changes to equilibrium structure are still seen from Table 16.2 to be much less than 10^{-3} Å. The relative energies of the defects are also changed by only 20 meV by this. This is a clear demonstration of the arguments regarding BSSE given in Section 16.2.1. We find this result to be a general feature of our procedure.

Also shown in Table 16.2 are the relative energies of the different structures. It is seen that the error associated with filtration is <10 meV and even the approximate filtration invokes errors of only 20 meV. These results are typical of a number of systems we have looked at. Although in an application of this in materials science, we would not consider publishing the relative energy from the approximate filtration but include it here to illustrate an important behaviour of the filtration (indeed, atom centred localised basis set calculations in general)—even if an approximation is used which produces gross (of order 10 eV) shifts in the absolute energy of structures, the relative energies remain converged and the structure is almost unchanged, indeed if bond lengths are published to three decimal places, they would appear unchanged. This can be exploited if desired as a means of accelerating structural optimisation, which typically consumes the majority of computing time in a research project.

As a second example, we have considered the binding of an interstitial oxygen atom O_i to a vacancy oxygen VO centre in silicon:

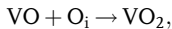


Table 16.2 Relative energies (ΔE) and errors in relaxed structures (Δ')—both mean (avg) and maximum (max) errors—of various defects in silicon (see text for details).

	ΔE (eV)	Δ'_{\max} (mÅ)	Δ'_{avg} (mÅ)
110 structure unfiltered	0.000	—	—
standard filtration	0.000	0.16	0.01
approx. filtration	0.000	0.68	0.06
T_d structure unfiltered	0.149	—	—
standard filtration	0.143	0.06	0.006
approx. filtration	0.162	0.41	0.05
H structure unfiltered	0.107	—	—
standard filtration	0.104	0.06	0.009
approx. filtration	0.125	0.28	0.046

where the VO_2 centre consists of two O atoms in a vacancy, each forming bonds to two of the silicon atoms and passivating the dangling bonds. In a calculation using Γ point sampling of the Brillouin zone, the binding energy is found to be 1.355 eV for the conventional algorithm and 1.354 eV for the filtered calculation, again showing a remarkable but nevertheless characteristic level of agreement between the two calculations.

Finally, we consider a defective metallic system, namely the ideal vacancy in aluminium. A 3^3 cell (108 atoms) with a relatively large primitive basis (*pddpp*) was used with a 10^3 uniform grid of points to perform integration over the Brillouin zone. To converge the formation energy to within ~ 0.01 eV required only ~ 50 min on a single core. We will shortly publish an extensive study of the accuracy of filtration algorithm for defects in a variety of systems.

16.5

Future Research Directions and Perspectives

In this section we wish to expand on previous discussions, assess their impact on the field and to address likely outcomes of on-going research in this exciting area. As well as significant improvements to speed and memory requirements, recent advances have presented a rich array of new questions and research directions that impact a very broad range of methods and applications. As this is a very rapidly evolving area we will spend sometime to discuss the impact of current research in the near-term.

There are some points that are immediately clear from the work presented or likely to be realised in the near-term:

- i) Tight binding calculations, which use conventional $O(N^3)$ diagonalisation methods, are only marginally faster than the full-DFT algorithm presented here.
- ii) Calculations involving structural relaxation or saddle-point location on systems containing $\sim 10\,000$ electrons are now comfortable on a single core.
- iii) The fact that the size of the primitive basis is decoupled from the size of the filtered basis allows for larger, and therefore more accurate, primitive sets to be used. On-going improvements to this procedure are likely to enable calculations—essentially at the basis set limit—at a cost comparable to tight binding.

The possibility of using low-complexity [a subset of these approaches are more commonly referred to as ‘linear-scaling’ or ‘ $O(N)$ ’] subspace kernels (such as the recursive bisection density matrix method [36]) rather than diagonalisation leaves open the question as to the ultimate relative performance of tight binding approaches compared to a full KSDFT calculation in the limit of a large number of atoms. This is due to a complex range of factors, such as matrix sparsity and spectral width, and their relation to accuracy.

16.5.1

Types of Calculations

Now, we shall discuss some broad types of calculations not only to highlight the progress that has been made but also to emphasise challenges that remain.

16.5.1.1 Thousands of Atoms on a Desktop PC

The ideal computational limit for the use of Gaussian orbitals combined with localised filter diagonalisation is large systems on a small number of cores due to memory efficiency and low operation count. As quad-core processors are currently rather common we are already at the stage where ~ 2000 silicon atoms can comfortably be handled on a single processor. Further algorithmic improvements coupled with the expected release of 8+ core processor promises to facilitate $\sim 4000+$ atom calculations on such machines in the near future. This computational limit also provides the perfect framework for calculations involving many independent subspace kernel calls, such as for separate k -points or calculation of the dynamical matrix. These can be effectively parallelised to allow the calculation of vibrational frequencies of ~ 1000 atom systems.

16.5.1.2 One Atom Per Processor

The opposite limit to performing large calculations on an inexpensive desktop machine is the ‘one atom per processor’ limit, in which we are interested in obtaining energies/forces of systems extremely rapidly by way of outstanding parallel scaling. Here, the interest is in using large capability supercomputing facilities to perform many interdependent calculations—the classic example being long time-scale molecular dynamics. As supercomputing facilities and architectures are leading to a rapid growth in the number of cores available to a calculation this is an important area of research. The current filter diagonalisation approach still has a direct diagonalisation kernel and therefore is not suited to this computational limit. However, virtually all other aspects of the calculation scale very well. Alternative algorithms for the subspace kernel will have to be developed to tackle this important class of problems.

At larger system sizes, the use of low-complexity methods, which inherently scale well, will largely tackle the problem of scaling. However, the size of the system where this will become realistically advantageous is not clear, and there will likely be an intermediate size range (up to several thousand atoms) where other strategies will be needed.

16.5.2

Prevailing Application Trends

We now turn to the impact discussions in the Section 16.5.1 are likely to have on the prevailing types of calculations performed by users of KSDFT methods.

In a recent work [7] it was shown that for silicon—a difficult example due to the fairly high atom/electron number ratio—the filtration algorithm was competitive with the conventional algorithm (using an accurate filtration radius of 12 a.u.) at 216 atoms. Indeed, with more approximate filtration (typically acceptable for force calculations) the filtration algorithm is essentially faster at any system size (Table 16.1).

We would consider the modelling of a defect in a 216 atom unit cell to be a fairly small calculation, but such calculations can rapidly become large. For example, some defects can have surprisingly long ranged strain effects and the use of cells of this size has produced erroneous conclusions (see for example Ref. [37]). Even though atoms far from a defect typically do not relax far from their perfect lattice site the number of such atoms in a shell of a given radius is large and therefore they have an effect on formation and migration energies and the like [38].

However, even point defect calculations can become demanding when tests of cell size convergence are required—doubling the distance between point defects in a 216 atom system would require the use of the 1728 atom unit cell discussed earlier. This would usually be regarded as a very ‘large’ (read ‘time consuming’) calculation by today’s standards. However, a glance back at Table 16.1 and we see that such a calculation is tractable, with approximate filtration, on a single core. In the cases of certain types of problem (*e.g.* charged defects) correction schemes [39–41] have been popular to avoid performing large calculations (*i.e.* to avoid reaching the cubic bottleneck). Such schemes should be viewed as complementary to performing large-scale calculations not a replacement for them.

Maybe the ease at which ~ 1000 – 2000 atoms calculations can now be performed will lead to a re-evaluation of many point defect problems where questions remain over the size of supercell used. Moving away from point defects to extended defects—the need for a few thousand atoms becomes even more necessary. The performance improvements here will enable a far greater complexity of problem to be treated, for engineering problems associated with imperfect interfaces; the interaction of defects with complex environments; a more accurate treatment of dislocations; their motion and interaction with one another and other defects. So, one could see methods able to perform accurate calculations containing several thousand atoms as opening the afore mentioned systems to the same level of scrutiny presently reserved for point defects.

16.5.3

Methodological Developments

The filtration algorithm represents a significant shift, indeed a sea change, in the speed and convenience of accurate KSDFT calculations for a range of systems sizes—but especially for large systems. It is evident that, in many respects, calculations involving a few thousand electrons present a comparable challenge—in terms of computational burden—per SCF iteration to a tight binding calculation.

However, we wish to stress, these implementations are still rather new. A great deal of scope exists, provided by these recent developments, for further optimisa-

tions. Also, due to the recent dramatic advances [6] parts of the code that previously were insignificant, therefore did not warrant particular attention from the point of view of further optimisation (such as the matrix build) have once again become an issue and work is being done to address these topics.

From a methodological development standpoint—just as conventional algorithms have aided the development of $\mathcal{O}(N)$ and low-complexity algorithms—these new methods will, in turn, be of significant use in the development of new multi-length-scale approaches, such as hybrid QM/MM modelling and the like [42–44], as direct theory to theory comparisons will be possible. It remains to be seen whether current hybrid approaches will be successfully, in most cases, verified or whether a ‘length scale drift’ will occur [as has certainly been the case for many $\mathcal{O}(N)$ methods] and in a few years we may be using full KSDFD for calculations now seen as the purview of more approximate methods. Certainly where important questions remain with such approaches—such as (i) How does one link the QM and MM regions and decide their respective boundaries?, (ii) How does one treat highly complex structures with no obvious reference point for MM such as the perfect crystal?, (iii) How does one cope with a system where the QM region becomes very large?, (iv) How does one assess the propagation of errors as one drifts from the ‘Kohn–Sham surface’? and (v) What is the chemical potential of the complete QM/MM system? In other words, how does one generate the correct QM state?—the use of a single, robust and tried and tested framework is certainly attractive, and worth striving for.

The fact that 1000 atom calculations are becoming comfortable in serial should, at once, put an end the oft expressed sentiment that Kohn–Sham density functional theory can only handle ‘a few hundred atoms at most’.

Although the use of low-complexity methods certainly will become important, it is clear that for realistic calculations the much commented upon crossover point—where a low-complexity algorithm becomes quicker than a conventional approach—is significantly larger than suggested by the early optimism in the literature. In fact, it is, to a large extent, nonsense now to talk of a crossover point between low-complexity and conventional approaches—we have already seen (in Section 16.4) a cubically scaling algorithm benefit hugely from the inclusion of ideas from low-complexity methodologies.

We now return to the issue of BSSE and the impact of the filtration algorithm on this problem. Clearly, in the large system limit the subspace diagonalisation as the final remaining $\mathcal{O}(N^3)$ operation dominates the calculation. As this diagonalisation is independent of the size of the primitive set, in the large system limit, large primitive sets—previously not used because of their severe impact on performance—can be used. This will increase the effort required in the filtration step, but this is currently insignificant (for large enough systems), scaling linearly with system size and taking just 3% of the total time for the 4096 atom system considered earlier. On-going improvements in this part of the algorithm, already well in hand, will reduce the system size at which this becomes an issue and should enable these calculations with localised orbitals to be (almost) systematically converged, even in routine runs. The fact that, in many respects, plane-wave accuracy for the cost of tight

binding seems to be achievable, and possibly even transparently to the user, makes this an exciting possibility.

16.6

Conclusions

A presentation of current and on-going developments in the AIMPRO code has been presented. The speed of KSDFT calculations using the latest state-of-the-art algorithms is comparable to a tight binding calculation. Even considering the extra memory and operations specimen examples such as 1000 silicon atoms on a single core are becoming comfortable and standard calculations.

Acknowledgement

The authors thank J. P. Goss and A. Lawson for useful discussions. M. J. R. gratefully acknowledges the support of the Alexander von Humboldt Foundation.

References

- 1 Kohn, W. and Sham, L.J. (1965) *Phys. Rev.*, **140**, A1133.
- 2 Hohenberg, P. and Kohn, W. (1964) *Phys. Rev.*, **136**, B864.
- 3 Jones, R. and Briddon, P.R., in: (1998), *Identification of Defects in Semiconductors, Vol. 51A of Semiconductors and Semimetals*, edited by M. Stavola, Academic Press, Boston, Chap. 6.
- 4 Briddon, P.R. and Jones, R. (2000) *Phys. Status Solidi B*, **217**, 131.
- 5 Rayson, M.J. and Briddon, P.R. (2008) *Comput. Phys. Commun.*, **178**, 128.
- 6 Rayson, M.J. and Briddon, P.R. (2009) *Phys. Rev. B*, **80**, 205104.
- 7 Rayson, M.J. (2010) *Comput. Phys. Commun.*, **181**, 1051.
- 8 Rayson, M.J. (2007) *Phys. Rev. E*, **76**, 026704.
- 9 Rayson, M.J. and Briddon, P.R. (2008) *Phys. Rev. B*, **77**, 035119.
- 10 Obara, S. and Saika, A. (1986) *J. Chem. Phys.*, **84**, 3963.
- 11 Lippert, G., Hutter, J. and Parrinello, M. (1999) *Theor. Chem. Acc.*, **103**, 124.
- 12 Kresse, G. and Furthmüller, J. (1996) *Phys. Rev. B*, **54**, 11169.
- 13 Vetterling, W.T. and Flannery, B.P. (2002) *Numerical Recipes*, second ed., edited by Press, and S.A. Teukolsky, (Cambridge University Press).
- 14 Farkas, O. and Schlegel, H.B. (2002) *Phys. Chem. Chem. Phys.*, **4**, 11.
- 15 Wardle, M.G., Goss, J.P., and Briddon, P.R. (2006) *Phys. Rev. Lett.*, **96**, 205504.
- 16 Wardle, M.G., Goss, J.P., and Briddon, P.R. (2005) *Phys. Rev. B*, **72**, 155108.
- 17 Wardle, M.G., Goss, J.P., and Briddon, P.R. (2005) *Phys. Rev. B*, **71**, 155205.
- 18 MacLeod, R.M., Murray, S.W., Goss, J.P., and Briddon, P.R. (2009) *Phys. Rev. B*, **80**, 054106.
- 19 Etnimi, K.M., Ahmed, M.E., Briddon, P.R., Goss, J.P., and Gsies, A.M. (2009) *Phys. Rev. B*, **79**, 205207.
- 20 Shaw, M.J., Briddon, P.R., Goss, J.P., Rayson, M.J., Kerridge, A., Harker, A.H., and Stoneham, A. M. (2005) *Phys. Rev. Lett.*, **95**, 105502.
- 21 Goss, J.P., Coomer, B.J., Jones, R., Shaw, T.D., Briddon, P.R., Rayson, M., and Öberg, S. (2001) *Phys. Rev. B*, **63**, 195208.

- 22 Rayson, M.J., Goss, J.P., and Briddon, P.R. (2003) *Physica B*, **340**, 673.
- 23 Goss, J.P., Jones, R., Shaw, T.D., Rayson, M.J., and Briddon, P.R. (2001) *Phys. Status Solidi A*, **186**, 215.
- 24 Goss, J.P., Briddon, P.R., Rayson, M.J., Sque, S.J., and Jones, R. (2005) *Phys. Rev. B*, **72**, 035214.
- 25 Goss, J.P., Rayson, M.J., Briddon, P.R., and Baker, J.M. (2007) *Phys. Rev. B*, **76**, 045203.
- 26 Coutinho, J., Jones, R., Briddon, P.R., and Öberg, S. (2000) *Phys. Rev. B*, **62**, 10824.
- 27 Wardle, M.G., Goss, J.P., and Briddon, P.R. (2006) *Appl. Phys. Lett.*, **88**, 261906.
- 28 Goss, J.P., Jones, R., and Briddon, P.R. (2002) *Phys. Rev. B*, **65**, 035203.
- 29 Liggins, S., Newton, M.E., Goss, J.P., Briddon, P.R., and Fisher, D. (2010) *Phys. Rev. B*, **81**, 085214.
- 30 Fall, C.J., Jones, R., Briddon, P.R., Blumenau, A.T., Frauenheim, T., and Heggie, M.I. (2002) *Phys. Rev. B*, **65**, 245304.
- 31 Fall, C.J., Blumenau, A.T., Jones, R., Briddon, P.R., Frauenheim, T., Gutierrez-Sosa, A., Bangert, U., Mora, A.E., Steeds, J.W., and Butler, J.E. (2002) *Phys. Rev. B*, **65**, 205206.
- 32 Ewels, C.P., Van Lier, G., Charlier, J.C., Heggie, M.I., and Briddon, P.R. (2006) *Phys. Rev. Lett.*, **96**, 216103.
- 33 Briddon, P.R. and Rayson, M.J. (in preparation).
- 34 Hartwigsen, C., Goedecker, S., and Hutter, J. (1998) *Phys. Rev. B*, **58**, 3641.
- 35 Monkhorst, H.J. and Pack, J.D. (1976) *Phys. Rev. B*, **13**, 5188.
- 36 Rayson, M.J. (2007) *Phys. Rev. B*, **75**, 153203.
- 37 Goss, J.P., Briddon, P.R., and Eyre, R.J. (2006) *Phys. Rev. B*, **74**, 245217.
- 38 Sulimov, V.B., Sushko, P.V., Edwards, A.H., Shluger, A.L., and Stoneham, A.M. (2002) *Phys. Rev. B*, **66**, 024108.
- 39 Makov, G. and Payne, M.C. (1995) *Phys. Rev. B*, **51**, 4014.
- 40 Lany, S. and Zunger, A. (2008) *Phys. Rev. B*, **78**, 235104.
- 41 Freysoldt, C., Neugebauer, J., and Van de Walle, C.G. (2009) *Phys. Rev. Lett.*, **102**, 016402.
- 42 Csanyi, G., Albaret, T., Payne, M.C., and De Vita, A. (2004) *Phys. Rev. Lett.*, **93**, 175503.
- 43 Buló, R.E., Ensing, B., Sikkema, J., and Visscher, L. (2009) *J. Chem. Theory Comput.*, **9**, 2212.
- 44 Gao, J.L. and Truhlar, D.G. (2002) *Annu. Rev., Phys. Chem.*, **53**, 467.